Materials Research Express

PAPER • OPEN ACCESS

Photocatalytic activity of $CuInS_2$ nanoparticles synthesized via a simple and rapid microwave heating process

To cite this article: Nawapong Chumha *et al* 2020 *Mater. Res. Express* **7** 015074

Materials Research Express

PAPER

Photocatalytic activity of $CuInS_2$ nanoparticles synthesized via a simple and rapid microwave heating process

Nawapong Chumha[1], **Watcharapong Pudkon**[1], **Auttaphon Chachvalvutikul**[1], **Tawanwit Luangwanta**[1], **Chamnan Randorn**[1,2,3], **Burapat Inceesungvorn**[1,2,3], **Athipong Ngamjarurojana**[4] and **Sulawan Kaowphong**[1,2,3]

[1] Department of Chemistry, Faculty of Science, Chiang Mai University, Chiang Mai 50200, Thailand
[2] Center of Excellence in Materials Science and Technology, Chiang Mai University, Chiang Mai 50200, Thailand
[3] Center of Excellence for Innovation in Chemistry, Faculty of Science, Chiang Mai University, Chiang Mai 50200, Thailand
[4] Department of Physics and Materials Science, Faculty of Science, Chiang Mai University, Chiang Mai 50200, Thailand

E-mail: sulawank@gmail.com **and** sulawan.k@cmu.ac.th

OPEN ACCESS

RECEIVED
12 October 2019

REVISED
29 November 2019

ACCEPTED FOR PUBLICATION
7 January 2020

PUBLISHED
20 January 2020

Keywords: $CuInS_2$, nanoparticles, microwave heating, photocatalyst, degradation

Supplementary material for this article is available online

Abstract

In this research, visible–light photocatalytic activities of $CuInS_2$ nanoparticles for degradation of three organic dyes (rhodamine B; RhB, methylene blue; MB, and methyl orange; MO) were investigated. The $CuInS_2$ nanoparticles were synthesized by a simple and rapid microwave heating process using sodium sulfide as a sulfur source and then characterized by x–ray diffraction (XRD), field emission scanning electron microscopy (FESEM), transmission electron microscopy (TEM), Brunauer–Emmett–Teller (BET), and UV–vis diffuse reflectance spectroscopy (UV–vis DRS) techniques. The synthesized $CuInS_2$ nanoparticles exhibited excellent photocatalytic degradation activity to the cationic dyes (RhB and MB) when compared with that of anionic dye (MO). Zeta potential of the $CuInS_2$ photocatalyst was measured to elucidate the adsorption ability toward dye molecules. A possible photocatalytic degradation mechanism was proposed based on active species quenching experiments and Mott–Schottky analysis.

1. Introduction

Semiconductor–mediated heterogeneous photocatalysis is a promising technology for energy and environmental applications [1–4]. Metal oxide semiconductors, such as TiO_2 and ZnO, have been widely used as photocatalysts for the degradation of organic contaminants in wastewater owing to their non–toxicity, and properties of chemical and thermal stability [5–8]. Unfortunately, these materials suffer from the poor utilization of visible light due to their large band gaps (3.2 eV for TiO_2 and 3.3 eV for ZnO) [5–8]. Binary metal sulfides are attractive candidates as highly efficient visible–light driven photocatalysts because the valence bands of these materials are constructed by 3*p* orbitals of S, which results in narrower band gaps when compared to those of the metal oxides, and thus make most of the metal sulfides sensitive to visible light [9]. However, these materials have lower charge separation efficiency and undergo photocorrosion, limiting their practical applications [10]. Recently, ternary metal sulfide–based photocatalysts have received increasing amounts of focus in photocatalysis research because of their large absorption coefficient over a wide spectral range, good thermal property, and long–term stability against photocorrosion when compared to relevant binary metal sulfide–based photocatalysts [11, 12]. Interestingly, the nanostructured photocatalysts that have large specific surface area possess more active sites for the favorable transport of electrons and holes to the surface of the photocatalysts which are available for photocatalytic reactions. All of which results in an improvement in photocatalytic performance in comparison to bulk materials [13].

Copper indium sulfide ($CuInS_2$) is an interesting ternary metal sulfide that has a wide range of potential applications including photocatalysis [14–18], in photodetectors [19], bioimaging [20, 21] and in solar cells

[22, 23]. Its conduction band is constructed from 5*s* orbital of In and its valence band consists of 3*p* orbitals of S [12]; thereby, a narrower band gap energy (1.53 eV for the bulk) can be achieved. In the photocatalysis, it has been explored as a photocatalyst for H_2 evolution [14, 15, 24, 25], organic pollutant degradation [16, 26, 27], and nitrate ion reduction [17, 18]. Hydro/solvothermal methods have been used to synthesize $CuInS_2$ nanoparticles [28–32]. However, these methods generally require expensive and complicated equipment, long periods of reaction time and high consumption of an electrical energy. Microwave heating synthesis is found to be an effective method for preparing nanomaterials over a short reaction time due to its high potential to pulse, which can generate a noticeable degree of heating inside the reaction system [33]. Our previous studies [23, 34] have reported on the microwave synthesis of the $CuInS_2$ nanostructures using thioacetamide and L–cysteine as sulfur sources. Despite the fact that $CuInS_2$ nanostructures were obtained, long periods of irradiation time were required (22.5 min). This could be caused by the partial loss of energy for cleaving the C–S bond in the thioacetamide molecules [23] and the metal–organic bonds in the metal–L–cysteine complexes [34] to release the sulfide (S^{2-}) ion to subsequently form the $CuInS_2$ nanoparticles.

In this research, we have reported on a cyclic microwave heating method for synthesizing $CuInS_2$ nanoparticles using sodium sulfide as a sulfur source. Since sodium sulfide is an ionic compound, it can more rapidly release sulfur ion rather than thioacetamide and L–cysteine which are a covalent compound. The required reaction time for the microwave synthesis of $CuInS_2$ nanostructures is expected to be relatively fast. The photocatalytic degradation activities of rhodamine B, methylene blue and methyl orange (representing organic pollutant) over the synthesized $CuInS_2$ photocatalyst were investigated. Mott–Schottky and active species quenching experiments were carried out in order to clarify a possible photocatalytic degradation mechanism.

2. Experimental procedure

2.1. Synthesis of $CuInS_2$ nanoparticles

All the chemicals were analytical grade and used without further purification. $CuCl_2 \cdot 2H_2O$ (2 mmol; BDH Chemicals, Ltd, 98%), $InCl_3 \cdot 4H_2O$ (2 mmol; Sigma–Aldrich, Co., 99.9%) and Na_2S (4 mmol; Carlo Erba, 99.99%) were separately dissolved in 10 ml of ethylene glycol (Carlo Erba, 99.5%). These solutions were mixed together at room temperature for 30 min. The mixed solution was then irradiated using a domestic microwave oven operated at a frequency of 2450 MHz with a power of 600 W for 2–15 processing cycles. Each cycle lasted 30 s for every 60 s intervals (at 50% of microwave power). Black powder was collected and washed with deionized water and ethanol, respectively. Finally, the powder was dried at 80 °C.

2.2. Characterizations

A Rigaku Miniflex II x–ray diffraction (XRD) spectrometer was used to determine the crystal structure, purity and crystallinity of the synthesized powders. Particle size and morphology of the powders were determined by a JEOL JSM–6335F field emission scanning electron microscope (FESEM) operating at 15 kV and a JEOL JEM–2010 transmission electron microscope (TEM) operating at 200 kV. The average diameter of the nanoparticles was determined using Image J software. Energy-dispersive x-ray (EDX) spectroscopy was used in conjunction with FESEM to analyte the elemental composition of the sample. A SHIMADZU UV-1800 UV-vis diffuse reflectance spectrophotometer (UV-vis DRS) was used to determine the optical properties of the sample. A specific surface area was obtained by using the Brunauer–Emmett–Teller method (BET, Autosorb1MP, Quantachrome).

A HORIBA nanopartica SZ–100 zeta potential analyzer was used to measure the zeta potential of the $CuInS_2$ nanoparticles. Briefly, 20 mg of $CuInS_2$ were dispersed in 100 ml of the ionic solution (1×10^{-3} molL^{-1} of KCl). The pH of the solution was adjusted to be within a range of 1 to 9 using 0.1 M HCl in the acidic range and 0.1 M NaOH in the basic range.

The Mott–Schottky plot was recorded on an electrochemical analyzer (Autolab PGSTAT, N–Series) equipped with a three–electrode system. Working electrode with 1 cm^2 of sample film was prepared as follows: 100 mg of the $CuInS_2$ powder was dispersed in a mixture of isopropanol and DI water for 20 min of sonication. After that, the mixed suspension was dropped on the FTO substrate and then dried at 70 °C overnight. Pt sheet and Ag/AgCl (3.0 M KCl) were used as a counter electrode and a reference electrode, respectively. Na_2SO_4 (0.5 M, pH $\sim$ 7) was used as an electrolyte solution. The Mott-Schottky measurement was carried out at an applied frequency of 1000 Hz in the dark with an AC amplitude of 10 mV and potential ranged from −1.2 to +1.2 V (versus Ag/AgCl). The following equation was used to convert the measured potential versus Ag/AgCl to NHE scale; $E_{NHE} = E_{Ag/AgCl} + E^{o}_{Ag/AgCl}$, where $E^{o}_{Ag/AgCl}$ (3.0 M KCl) = 0.209 V at 25 °C.

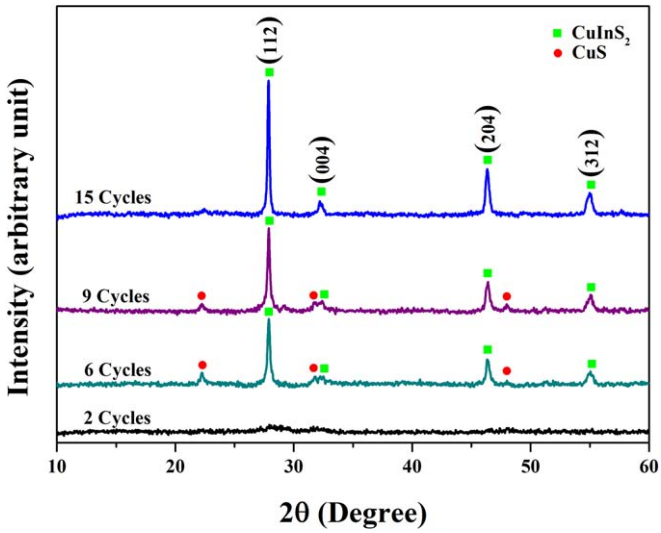

Figure 1. XRD patterns of the $CuInS_2$ powders synthesized at 600 W using different processing cycles.

2.3. Photocatalytic degradation experiment

$CuInS_2$ photocatalyst (100 mg) was dispersed in an aqueous solution of three organic dyes (rhodamine B, methylene blue, and methyl orange; 200 ml, 10 ppm). The suspension was magnetically stirred under dark conditions for 30 min to ensure that an equilibrium was reached between the adsorption and desorption on the surface of the $CuInS_2$ photocatalyst. The suspension was then irradiated under a 50 W light–emitting diode (LED) lamp for 0–360 min. The spectral irradiance of the LED light is shown in figure S1. The LED lamp exhibits a white light with the wavelength ranging from 400 to 700 nm, corresponding to a visible light region. The dye solution (5 ml) was taken after every 30 min of irradiation and then monitored using the UV–vis DRS spectrophotometer (SHIMADZU UV–1800) to determine the residual dye concentration. A blank experiment was carried out under visible light irradiation to verify that the decolorization of the dye was indeed due to the photocatalytic reaction. Decolorization efficiency of the photocatalyst was calculated from the changes in the intensity of the characteristic absorption peaks at the absorption maximum of the dyes (λ_{max} = 554, 664 and 464 nm for RhB, MB and MO, respectively) by applying the following equation;

$$Decolorization\ efficiency\ (\%) = \frac{C_0 - C}{C_0} \times 100$$

where C_0 represents the initial concentration of the maximum peak of the absorption spectrum, and C represents the residual dye concentration at each irradiated time interval.

3. Results and discussion

XRD patterns of the powders synthesized at 600 W using different processing cycles are shown in figure 1. No diffraction peak is observed from the XRD pattern of the powder synthesized at 2 cycles, implying that $CuInS_2$ crystals has not yet been formed. After being proceeded for 6 and 9 cycles, the diffraction peaks at 2θ of 27.87°, 46.37° and 55.01°, respectively, indexed to the (112), (204) and (312) planes of a tetragonal $CuInS_2$ structure (JCPDS database no. 32–0339), are found to be in a majority with the existence of a hexagonal CuS structure (JCPDS database no. 01–1281). It should be noted that measured temperatures of the reaction solutions irradiated at 6 and 9 cycles (3 and 4.5 min of irradiation, respectively) are 137 and 148 °C (figure 2), respectively. Herein, the XRD results are consistent with the results of previous reports [23, 35] which stated that CuS coexists with $CuInS_2$ when the temperature is lower than 160 °C. However, the diffraction peak intensity of the $CuInS_2$ phase becomes gradually stronger while that of the CuS phase is decreased with increasing processing cycles, indicating the improved purity and crystallinity of the $CuInS_2$ crystals. After the reaction process has been prolonged to 15 cycles (7.5 min of irradiation, 163 °C), pure $CuInS_2$ with highly crystalline is obtained. When compared with our previous reports [23, 34], the synthesis of the $CuInS_2$ powder using Na_2S as a sulfur source requires considerably lower processing times under the same microwave power (600 W). This outcome can probably be attributed to the rapid release rate of S^{2-} ion from the ionic Na_2S compound. When Na_2S is dissolved in the polar solvent, S^{2-} ion is immediately released [36] and subsequently reacts with Cu^{2+} to form CuS nuclei, which is further reduced to Cu^{+} by ethylene glycol under microwave heating. Finally, the Cu^{+} reacts

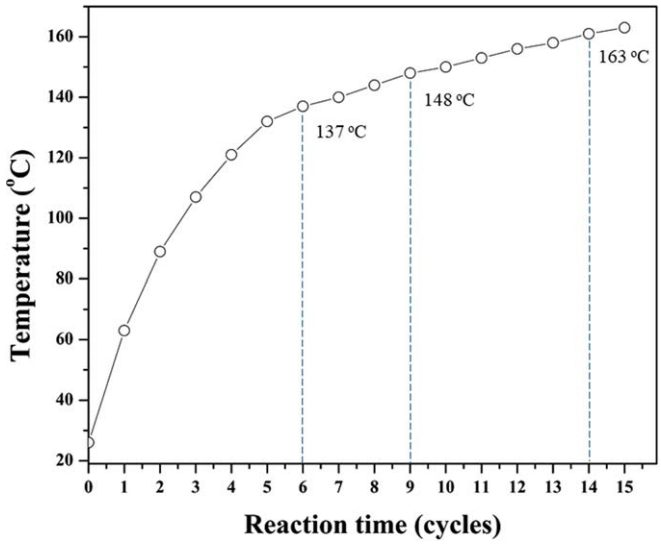

Figure 2. Measured temperatures of the irradiated solutions recorded at 600 W for different processing cycles during the microwave heating process.

with In^{3+} and S^{2-} in the solution to produce $CuInS_2$ crystals [23]. The size of the $CuInS_2$ crystals was calculated using the Debye–Scherrer's formula [37];

$$D = \frac{K}{\beta \cos \theta}$$

where D is the crystallite size in nanometer, λ is the wavelength of CuK_α radiation, β is the full width at half–maximum (FWHM) in radian, and θ represents the half–diffraction angle in degree. Scherrer's constant (K) was derived in Scherrer's original paper with $K = 2[\ln(2)/\pi]^{1/2}$ [38, 39], and a value of 0.94 was obtained for FWHM of the spherical crystals with cubic symmetry [39]. Although the Scherrer equation was derived for the material of the cubic crystals, it is usually used to estimate the crystallite sizes of both cubic and noncubic materials [38]. The calculated average crystallite size is 65 nm. Lattice parameters of $CuInS_2$ were calculated by assessing the relationship between the Bragg diffraction spacing and tetragonal cell parameters [40] as follows:

$$d_{hkl} = \frac{a}{\sqrt{h^2 + k^2 + l^2(a/c)^2}}$$

where d_{hkl} is the Bragg diffraction spacing for the (hkl) plane, $h\,k\,l$ are the miller indices, and a and c are the lattice parameters. The calculated lattice parameters of the $CuInS_2$ nanoparticles are $a = b = 5.5310$ Å and $c = 11.1104$ Å, which agree well with those of the corresponding JCPDS database ($a = b = 5.5170$ Å and $c = 11.0600$ Å).

FESEM image of the $CuInS_2$ powder synthesized at 15 cycles are shown in figure 3(a). The $CuInS_2$ powder is composed of nanoparticles with diameters in a range of 30–65 nm, and this is consistent with the TEM image presented in figure 3(b). The corresponding high-magnification TEM image (figure 3(c)) shows a lattice fringe with a spacing of 0.20 nm, which corresponds to the (204) plane of the tetragonal phase of $CuInS_2$. The SAED pattern (figure 3(d)) shows bright concentric rings that are indicative of the tetragonal $CuInS_2$ phase, which corresponds well with the XRD pattern shown in figure 1. Moreover, the EDX spectrum of $CuInS_2$ (figure 2(e)) appears the characteristic signals of Cu, In, S, Al, Au and C elements. It should be noted that the signals of the Al, Au and C elements come from the aluminium supporting holder, coated gold, and environment, respectively. The results obtained from the SAED and EDX analyses further indicate the purity of the $CuInS_2$ crystals. Analyzed by the degree of BET adsorption–desorption of nitrogen gas at the temperature of liquid nitrogen, the specific surface area of the $CuInS_2$ nanoparticles is recorded at 31.64 m^2g^{-1}.

UV–vis DRS spectrum of the $CuInS_2$ powder synthesized at 600 W for 15 cycles is shown in figure 4(a). The band gap energy of $CuInS_2$ can be calculated by the plot of transformed Kubelka−Munk function $(F(R).h\nu)^2$ versus photon energy $h\nu$ [41], where R represents the proportion of light reflected, h is the Planck's constant and ν is the photon frequency. As illustrated in the inset of figure 4, the band gap energy of $CuInS_2$ was calculated as 1.40 eV. This implies that the $CuInS_2$ nanoparticles have an ability to absorb visible light, suggesting a promising use of this nanomaterial as a visible light active photocatalyst. To determine the flat–band potential (E_f) of $CuInS_2$, Mott–Schottky measurement was performed at a frequency of 1000 Hz and potential ranged from −1.2 to +1.2 V (versus Ag/AgCl). Figure 4(b) shows the negative slope of the Mott–Schottky plot of the $CuInS_2$

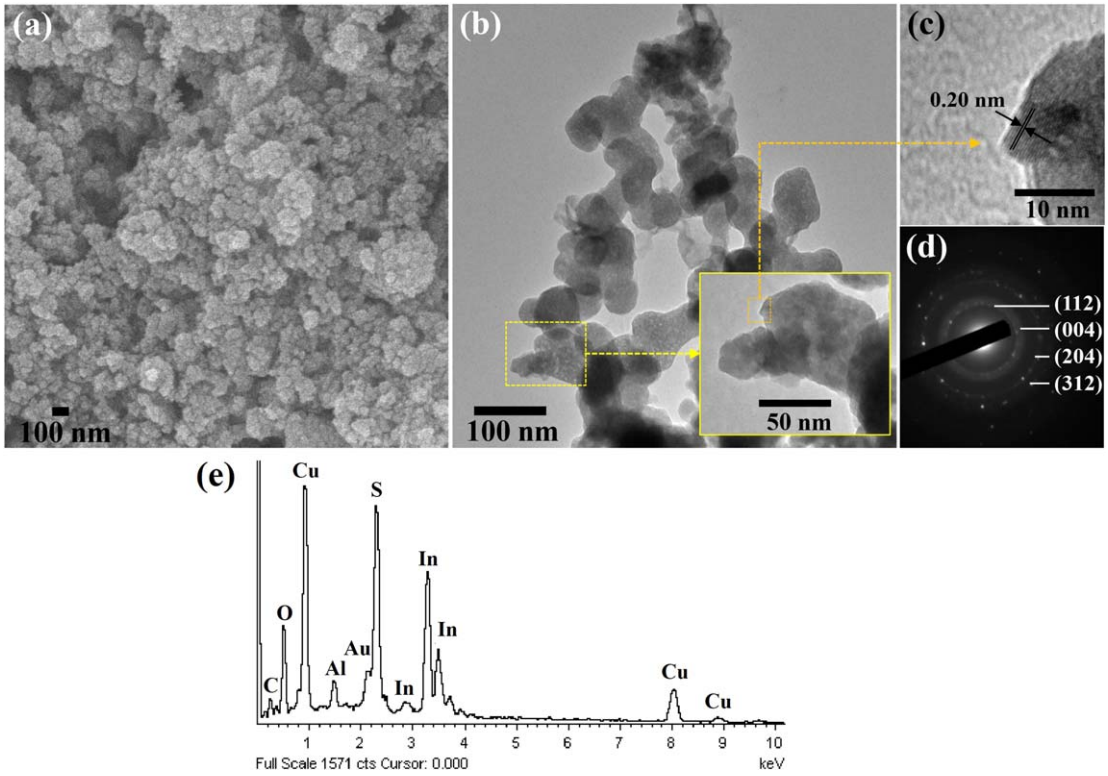

Figure 3. (a) FESEM (b) TEM and (c) high-magnification TEM images of the $CuInS_2$ powder. (d) the corresponding SAED pattern and (e) EDX spectrum.

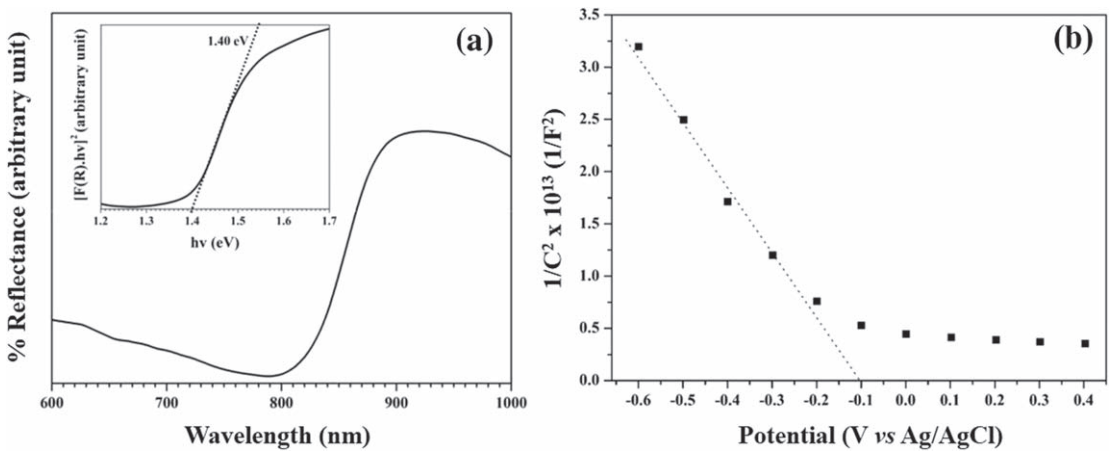

Figure 4. (a) UV–vis DRS spectrum of the $CuInS_2$ nanoparticles. Inset of (a): Kubelka−Munk−transformed diffuse reflectance spectrum of the $CuInS_2$ nanoparticles. (b) Mott–Schottky plot of the $CuInS_2$ electrode in 0.5 M Na_2SO_4 aqueous solution with a frequency of 1000 Hz.

electrode, indicating that $CuInS_2$ is a p–type semiconductor. In addition, the flat band potential (E_f) of $CuInS_2$ is −0.10 V (versus Ag/AgCl), which corresponds to 0.11 V (versus NHE). Generally, the flat band potential of the p–type semiconductors is about 0.1 V more negative than the valence band (VB) potential [42]. Therefore, the VB potential of $CuInS_2$ was estimated to be 0.21 V versus NHE. Consequently, based on its E_g (figure 4(a)), the conduction band (CB) potential was calculated to be −1.19 V versus NHE. Notably, the Mott–Schottky plot was also carried out at a frequency of 100 Hz on the same electrochemical analyzer. The Mott–Schottky plot shown in the supporting information (figure S2) reveals the negative slope with the flat band potential (E_f) of −0.15 V (versus Ag/AgCl), which is close to the E_f value obtained from the Mott–Schottky plot at 1000 Hz.

Decolorization efficiencies of RhB, MB and MO with and without the $CuInS_2$ photocatalyst are shown in figure 5(a). In the absence of the $CuInS_2$ photocatalyst, the photolysis of RhB, MB, and MO dyes by visible light is

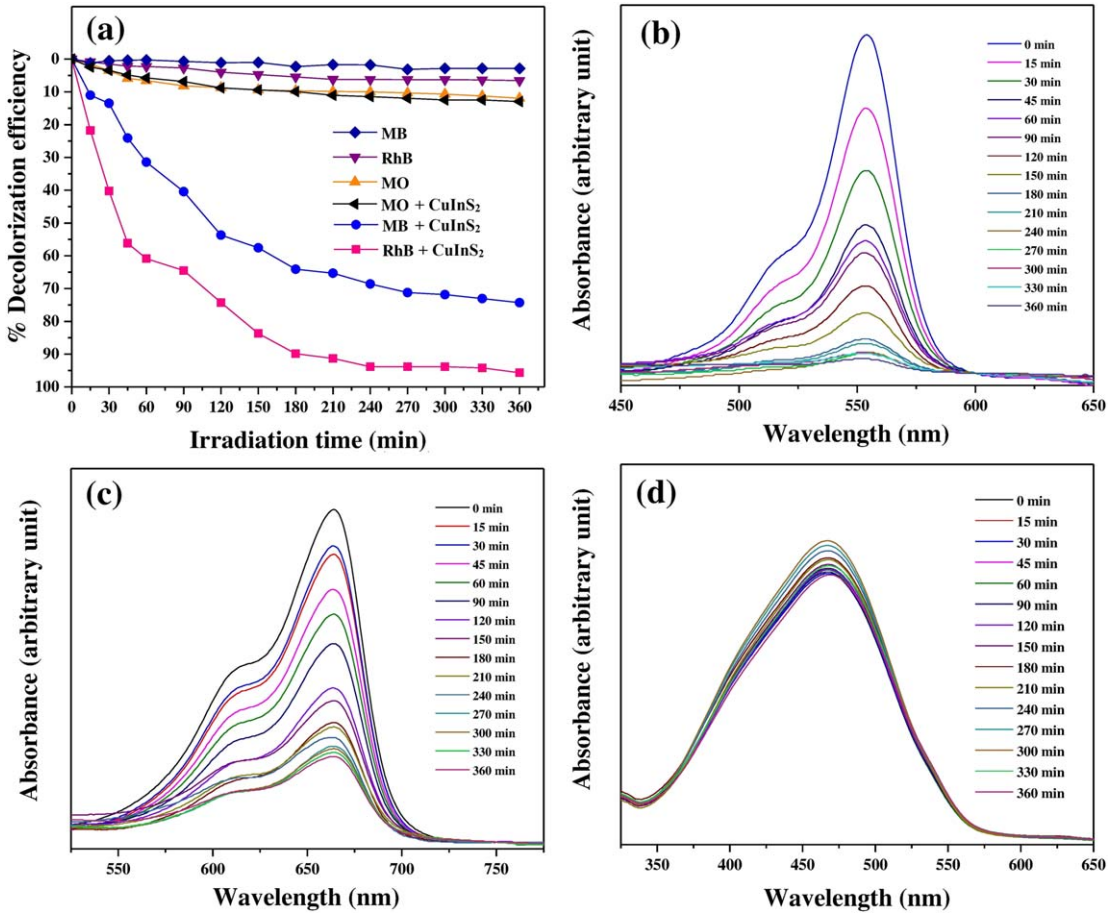

Figure 5. (a) Decolorization efficiency (%) of RhB, MB and MO with and without the $CuInS_2$ photocatalyst. Changes in the absorption intensity of (b) RhB, (c) MB and (d) MO in the presence of the $CuInS_2$ photocatalyst under visible light irradiation.

only 7.67, 2.96, and 11.94%, respectively, indicating that the self–photodegradations of these dyes are very slow and negligible under visible light. In the presence of the $CuInS_2$ photocatalyst, the $CuInS_2$ photocatalyst degrades MB and RhB by up to 64.08% and 74.29% within 180 min, respectively, and the decolorizations of MB and RhB are almost completed when the irradiation is continued up to 360 min (91.21% for MB and 97.80% for RhB). Surprisingly, only 12.96% of MO is decolorized, which is found to be quite close to its level of photolysis suggesting the high selectivity of the $CuInS_2$ photocatalyst toward cationic dyes. The changes in the absorption intensity of RhB, MB and MO dyes that occur as a function of time in the presence of the $CuInS_2$ photocatalyst under visible light irradiation are shown in figures 5(b)–(d), respectively. Under visible light irradiation, two competitive processes take place simultaneously during the photocatalytic degradations of the dyes; *N*–de–alkylation and destruction of the chromophore structure. The absorption intensity of the peaks of the dyes gradually decreases upon increasing irradiation time without detection of any new peaks and shifts of the absorption maximum. This implies that the dyes are continuously degraded during the photocatalytic processes through the chromophore destruction [43–45].

To elucidate the surface charge of photocatalyst nanoparticles, the zeta potential of the $CuInS_2$ photocatalyst at different pH solutions was measured for an isoelectric point determination. As is shown in figure 6, the pH value at the isoelectric point, $pH_{(IEP)}$, of the $CuInS_2$ photocatalyst is 3.27. Therefore, under our testing conditions in which the pH values of the RhB, MB and MO solutions in the presence of $CuInS_2$ are 3.86, 3.95, and 3.85, respectively, the $CuInS_2$ photocatalyst has a negative charge on its surface. As a result, the cationic dyes (RhB and MB) could be easily attached on the negatively charged surface of the $CuInS_2$ photocatalyst due to the electrostatic attraction force between them, thereby could promote photodegradation activity more effectively than the anionic dye (MO). The kinetics of the RhB and MB degradations by the $CuInS_2$ photocatalyst followed the pseudo–first–order model as is shown in the following equation [46];

$$\ln \frac{C_0}{C} = kt$$

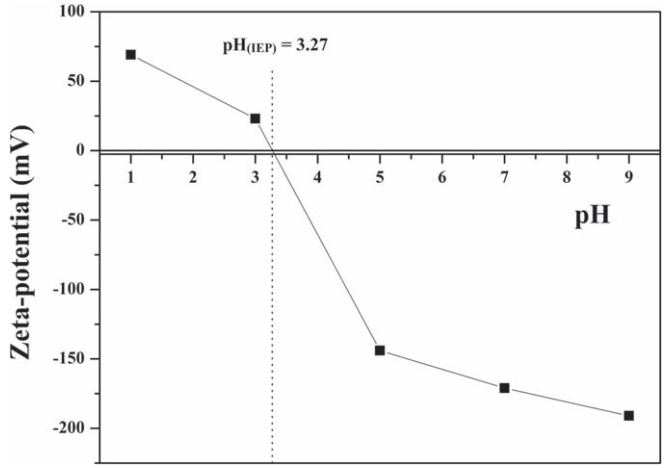

Figure 6. Zeta potential of the $CuInS_2$ nanoparticles at different pH solutions.

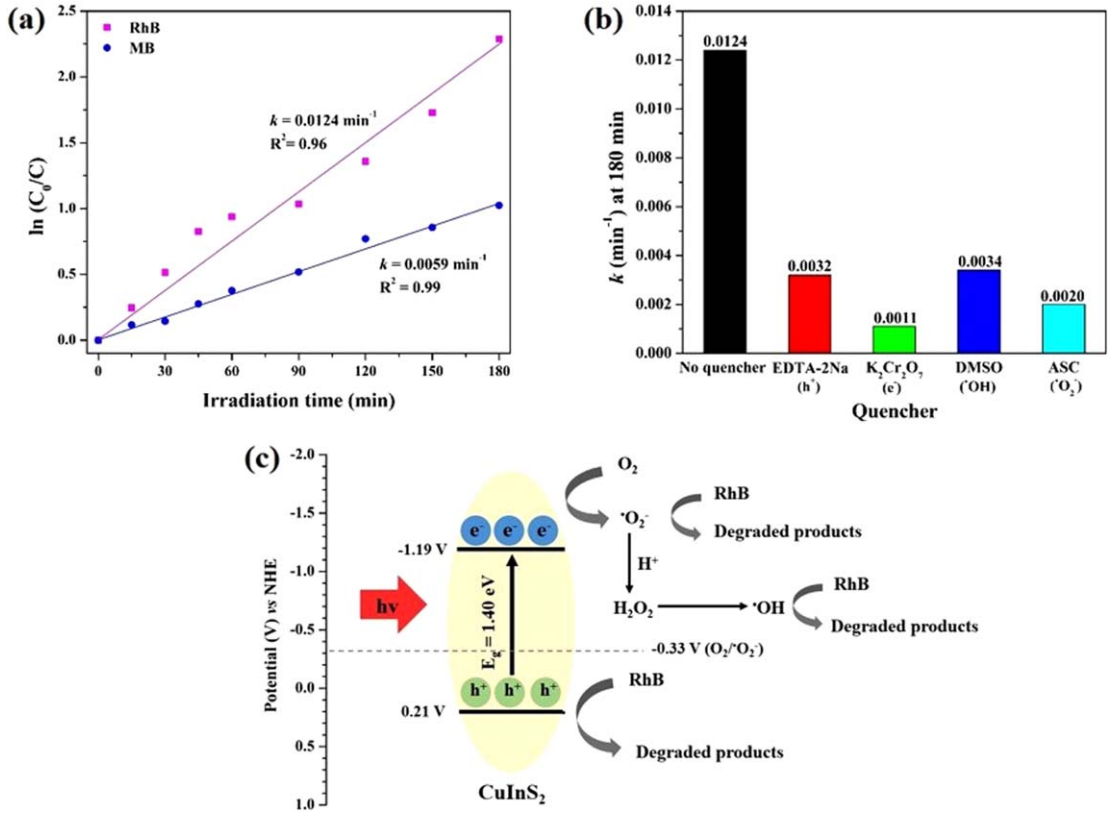

Figure 7. (a) A comparison of photocatalytic decolorization kinetics of RhB and MB in the presence of the $CuInS_2$ photocatalyst. (b) Effect of different quenchers on the decolorization efficiency of RhB over the $CuInS_2$ photocatalyst. (c) Energy band positions and possible photocatalytic degradation mechanism under visible light irradiation.

where C_0 is the initial concentration of dye and C is the concentration at the irradiation time (t). As is shown in figure 7(a), the initial rate constants (k) with the coefficient of determination (R^2), calculated from the initial slope of the fitted line between $\ln(C_0/C)$ and irradiation time (0–180 min), are 1.24×10^{-2} min^{-1} for RhB with $R^2 = 0.96$, and 0.59×10^{-3} min^{-1} for MB with $R^2 = 0.99$. These results confirm that the degradation of RhB is faster than that of MB. Under the same photocatalytic degradation pathway of RhB and MB, the faster photocatalytic degradation of RhB is probably due to the different frontier molecular orbital energies of RhB and MB [47]. The lowest unoccupied molecular orbitals (LUMOs) energy level of RhB is more positive than that of MB. Therefore, the higher the LUMOs energy level is favorable for the excited electrons to transfer from the LUMOs energy level of the RhB molecules to the conduction band of the semiconductor and thus, facilitate the photodegradation reaction process [48].

Figure 7(b) shows the quenching experiments used to investigate the active species involved in the photodegradation process of RhB over the $CuInS_2$ photocatalyst. Disodium ethylenediaminetetraacetate (EDTA–2Na, 1 mM), potassium dichromate ($K_2Cr_2O_7$, 1 mM), dimethyl sulfoxide (DMSO, 1 mM), and ascorbic acid (AA, 1 mM) were used to trap the hole (h^+), electron (e^-), hydroxyl radical (·OH) and superoxide radical ($\cdot O_2^-$), respectively. The additions of these quenchers decrease the kinetic rates of RhB, implying that h^+, e^-, ·OH and $\cdot O_2^-$ are the active species in the photodecolorization of RhB. Based on the experimental results, the energy band positions and possible photocatalytic degradation mechanism have been proposed in figure 7(c). After the $CuInS_2$ photocatalyst is exposed to visible light, electrons (e^-) in the valence band (VB) of the $CuInS_2$ photocatalyst are excited to the conduction band (CB) leaving holes (h^+) in the VB. The photogenerated e^- and h^+ then migrate to the surface of the photocatalyst in order to undergo photocatalytic reactions. The e^- accumulated at CB of $CuInS_2$ efficiently reduce dissolved O_2 in the solution to $\cdot O_2^-$ radical because the CB potential of the $CuInS_2$ (−1.19 V) is more negative than the reduction potential of $O_2/\cdot O_2^-$ (−0.33 V versus NHE). In addition, since the reduction potential of O_2/H_2O_2 is 0.695 V (versus NHE), the e^- can react with O_2 and H^+ to produce H_2O_2 which would then further produce ·OH radicals in the photocatalytic reaction [49–52]. These explanations correspond with the significant decreases that take place in the kinetic rate of RhB after the addition of $K_2Cr_2O_7$ quencher into the reaction solution. The h^+ that occurred on the VB of $CuInS_2$ cannot oxidize the H_2O molecules or OH^- to produce ·OH radicals since the VB potential of $CuInS_2$ (+0.21 V) is lower than the standard potentials of $\cdot OH,H^+/H_2O$ (2.72 V versus NHE) and $\cdot OH/OH^-$ (1.99 V versus NHE). Therefore, ·OH radicals can be generated by further reduction of $\cdot O_2^-$ radicals, as has been mentioned above. Finally, the $\cdot O_2^-$ and ·OH radicals oxidize the dye molecules to yield the final products such as CO_2, H_2O and etc [50]. Simultaneously, the h^+ in the VB of $CuInS_2$ can directly degrade the dye molecules. The mechanism for the degradation of dye molecules via $\cdot O_2^-$, ·OH, or the direct h^+ oxidation pathway is given by the following equations;

$$CuInS_2 + hv\ (visible\ light) \rightarrow CuInS_2\ (e_{CB}^- + h_{VB}^+) \quad (1)$$

$$CuInS_2(e_{CB}^-) + O_2 \rightarrow CuInS_2 + \cdot O_2^- \quad (2)$$

$$\cdot O_2^- + e^- + 2H^+ \rightarrow H_2O_2 \quad (3)$$

$$H_2O_2 + e^- \rightarrow \cdot OH + OH^- \quad (4)$$

$$\cdot O_2^- + \cdot OH + CuInS_2(h_{VB}^+) + Dye \rightarrow products \quad (5)$$

4. Conclusions

Pure and highly crystalline $CuInS_2$ nanoparticles were successfully synthesized through a simple and rapid microwave heating process using sodium sulfide as a sulfur source, which only required 7.5 min of microwave irradiating. This photocatalyst showed higher photocatalytic activity on the cationic dyes (RhB and MB) than on the anionic dye (MO), which was attributed to the electrostatic attraction between the cationic dye molecules and the negative charge on the photocatalyst's surface. The quenching tests indicated that h^+, e^- $\cdot O_2^-$ and ·OH were responsible for the photodegradation process. The results suggested that the $CuInS_2$ nanoparticles could be a potential photocatalyst for the degradation of organic pollutants in wastewater under visible light. In addition, this synthesis method is expected to be applicable to the preparation of other ternary chalcogenide nanomaterials.

Acknowledgments

This research is partially supported by Chiang Mai University. Additionally, financial support obtained from the Center of Excellence for Innovation in Chemistry (PERCH–CIC), Ministry of Higher Education, Science, Research and Innovation is gratefully acknowledged.

Data availability statement

The data that support the findings of this study are available from the corresponding author upon reasonable request. The data are not publicly available for legal and/or ethical reasons.

Conflict of Interest

The authors declare that they have no conflict of interest.

ORCID iDs

Sulawan Kaowphong https://orcid.org/0000-0003-2461-4421

References

[1] Fox M A 1983 Organic heterogeneous photocatalysis: chemical conversions sensitized by irradiated semiconductors *Acc. Chem. Res.* **16** 314–21
[2] Cherevatskaya M and König B 2014 Heterogeneous photocatalysts in organic synthesis *Russ. Chem. Rev.* **83** 183–95
[3] Mills A and Le Hunte S 1997 An overview of semiconductor photocatalysis *J. Photochem. Photobiol. A Chem.* **108** 1–35
[4] Ajmal A, Majeed I, Malik R N, Idriss H and Nadeem M A 2014 Principles and mechanisms of photocatalytic dye degradation on TiO_2 based photocatalysts: a comparative overview *RSC Adv.* **4** 37003–26
[5] Nakata K and Fujishima A 2012 TiO_2 photocatalysis: design and applications *J. Photochem. Photobiol. C Photochem. Rev.* **13** 169–89
[6] Schneider J, Matsuoka M, Takeuchi M, Zhang J, Horiuchi Y, Anpo M and Bahnemann D W 2014 Understanding TiO_2 photocatalysis: mechanisms and materials *Chem. Rev.* **114** 9919–86
[7] Hashimoto K, Irie H and Fujishima A 2005 $\{TiO\}_2$ photocatalysis: a historical overview and future prospects *Jpn. J. Appl. Phys.* **44** 8269–85
[8] Ong C B, Ng L Y and Mohammad A W 2018 A review of ZnO nanoparticles as solar photocatalysts: Synthesis, mechanisms and applications *Renew. Sustain. Energy Rev.* **81** 536–51
[9] Haque F, Daeneke T, Kalantar-zadeh K and Ou J Z 2017 Two-dimensional transition metal oxide and chalcogenide-based photocatalysts *Nano-Micro Lett.* **10**
[10] Zhang H and Zhu Y 2010 Significant visible photoactivity and antiphotocorrosion performance of CdS photocatalysts after monolayer polyaniline hybridization *J. Phys. Chem.* C **114** 5822–6
[11] Chuang P-H, Lin C C and Liu R-S 2014 Emission-tunable $CuInS_2$/ZnS quantum dots: structure, optical properties, and application in white light-emitting diodes with high color rendering index *ACS Appl. Mater. Interfaces* **6** 15379–87
[12] Regulacio M D and Han M-Y 2016 Multinary I-III-VI_2 and I_2-II-IV-VI_4 Semiconductor nanostructures for photocatalytic applications *Acc. Chem. Res.* **49** 511–9
[13] Adhikari S P and Lachgar A 2016 Effect of particle size on the photocatalytic activity of $\{BiNbO\}_4$ under visible light irradiation *J. Phys. Conf. Ser.* **758** 12017
[14] Zheng L, Xu Y, Song Y, Wu C, Zhang M and Xie Y 2009 Nearly monodisperse $CuInS_2$ hierarchical microarchitectures for photocatalytic H_2 evolution under visible light *Inorg. Chem.* **48** 4003–9
[15] Yuan Y-J, Chen D-Q, Huang Y-W, Yu Z-T, Zhong J-S, Chen T-T, Tu W-G, Guan Z-J, Cao D-P and Zou Z-G 2016 MoS_2 Nanosheet-modified $CuInS_2$ photocatalyst for visible-light-driven hydrogen production from water *ChemSusChem* **9** 1003–9
[16] Yu C, Zhang L, Tian L, Liu D, Chen F and Wang C 2014 Synthesis and formation mechanism of $CuInS_2$ nanocrystals with a tunable phase *CrystEngComm* **16** 9596–602
[17] Wang Y, Yang J, Gao W, Cong R and Yang T 2014 Organic-free hydrothermal synthesis of chalcopyrite $CuInS_2$ and its photocatalytic activity for nitrate ions reduction *Mater. Lett.* **137** 99–101
[18] Yue M, Wang R, Ma B, Cong R, Gao W and Yang T 2016 Superior performance of $CuInS_2$ for photocatalytic water treatment: full conversion of highly stable nitrate ions into harmless N_2 under visible light *Catal. Sci. Technol.* **6** 8300–8
[19] Bulyarsky S V, Vostretsova L N and Gavrilov S A 2016 Photodetectors based on $CuInS_2$ *Semiconductors* **50** 106–11
[20] Liu L, Hu R, Law W-C, Roy I, Zhu J, Ye L, Hu S, Zhang X and Yong K-T 2013 Optimizing the synthesis of red- and near-infrared $CuInS_2$ and $AgInS_2$ semiconductor nanocrystals for bioimaging *Analyst* **138** 6144–53
[21] Deng D, Chen Y, Cao J, Tian J, Qian Z, Achilefu S and Gu Y 2012 High-quality $CuInS_2$/ZnS quantum dots for *in vitro* and *in vivo* bioimaging *Chem. Mater.* **24** 3029–37
[22] Nakabayashi T, Miyazawa T, Hashimoto Y and Ito K 1997 Over 10% efficient $CuInS_2$ solar cell by sulfurization *Sol. Energy Mater. Sol. Cells* **49** 375–81
[23] Chumha N, Thongtem T, Thongtem S, Tantraviwat D, Kittiwachana S and Kaowphong S 2016 A single-step method for synthesis of $CuInS_2$ nanostructures using cyclic microwave irradiation *Ceram. Int.* **42** 15643–9
[24] Kobayakawa K, Teranishi A, Tsurumaki T, Sato Y and Fujishima A 1992 Photocatalytic activity of $CuInS_2$ and $CuIn_5S_8$ *Electrochim. Acta* **37** 465–7
[25] Luo J, Tilley S D, Steier L, Schreier M, Mayer M T, Fan H J and Grätzel M 2015 Solution transformation of Cu_2O into $CuInS_2$ for solar water splitting *Nano Lett.* **15** 1395–402
[26] Yang Y, Que W, Zhang X, Xing Y, Yin X and Du Y 2016 Facile synthesis of ZnO/$CuInS_2$ nanorod arrays for photocatalytic pollutants degradation *J. Hazard. Mater.* **317** 430–9
[27] Liu R, Liu Y, Liu C, Luo S, Teng Y, Yang L, Yang R and Cai Q 2011 Enhanced photoelectrocatalytic degradation of 2,4-dichlorophenoxyacetic acid by $CuInS_2$ nanoparticles deposition onto TiO_2 nanotube arrays *J. Alloys Compd.* **509** 2434–40
[28] Wochnik A S, Frank A, Heinzl C, Häusler J, Schneider J, Hoffmann R, Matich S and Scheu C 2013 Insight into the core–shell structures of Cu–In–S microspheres *Solid State Sci.* **26** 23–30
[29] Peng S, Cheng F, Liang J, Tao Z and Chen J 2009 Facile solution-controlled growth of $CuInS_2$ thin films on FTO and TiO_2/FTO glass substrates for photovoltaic application *J. Alloys Compd.* **481** 786–91
[30] Long F, Wang W-M, Tao H, Jia T, Li X-M, Zou Z and Fu Z 2010 Solvothermal synthesis, nanocrystal print and photoelectrochemical properties of $CuInS_2$ thin film *Mater. Lett.* **64** 195–8
[31] Han S, Kong M, Guo Y and Wang M 2009 Synthesis of copper indium sulfide nanoparticles by solvothermal method *Mater. Lett.* **63** 1192–4
[32] Feng J, Han J and Zhao X 2009 Synthesis of $CuInS_2$ quantum dots on TiO_2 porous films by solvothermal method for absorption layer of solar cells *Prog. Org. Coatings* **64** 268–73

[33] Zhu Y-J and Chen F 2014 Microwave-assisted preparation of inorganic nanostructures in liquid phase *Chem. Rev.* **114** 6462–555
[34] Chumha N, Thongtem T, Thongtem S, Kittiwachana S and Kaowphong S 2018 Cyclic microwave radiation synthesis, photoconductivity, and optical properties of $CuInS_2$ hollow sub-microspheres *Appl. Surf. Sci.* **447** 292–9
[35] Qi Y, Tang K, Zeng S and Zhou W 2008 Template-free one-step fabrication of porous $CuInS_2$ hollow microspheres *Microporous Mesoporous Mater.* **114** 395–400
[36] Yadav S, Shrivas K and Bajpai P K 2019 Role of precursors in controlling the size, shape and morphology in the synthesis of copper sulfide nanoparticles and their application for fluorescence detection *J. Alloys Compd.* **772** 579–92
[37] Suryanarayana C and Norton M G 1998 Determination of Crystallite Size and Lattice Strain *X-Ray Diffraction: A Practical Approach* ed C Suryanarayana and M G Norton (Springer Science & Business Media) 978-1-4899-0148-4 (https://doi.org/10.1007/978-1-4899-0148-4)
[38] Patterson A L 1939 The Scherrer formula for x-ray particle size determination *Phys. Rev.* **56** 978–82
[39] Warren B E 1990 *X-Ray Diffraction* (New York, United States of America: Dover Publications) 139780486663173
[40] Hargittai I 2009 Christopher Hammond: the basics of crystallography and diffraction. Third edition *Struct. Chem.* **20** 751
[41] El-Sheikh S M, Khedr T M, Zhang G, Vogiazi V, Ismail A A and O'Shea K 2017 Tailored synthesis of anatase–brookite heterojunction photocatalysts for degradation of cylindrospermopsin under UV–Vis light *Chem. Eng. J.* **310** 428–36
[42] Zhang Y, Jin Z, Yuan H, Wang G and Ma B 2018 Well-regulated nickel nanoparticles functional modified ZIF-67 (Co) derived Co_3O_4/CdS p-n heterojunction for efficient photocatalytic hydrogen evolution *Appl. Surf. Sci.* **462** 213–25
[43] Khlyustova A and Subbotkina I 2012 Kinetic regularities of methylene blue destruction processes in different media under the impact of the diaphragm discharge plasma *High Temp. Mater. P-US* **16** 71–9
[44] Liu T, Wang L, Lu X, Fan J, Cai X, Gao B, Miao R, Wang J and Lv Y 2017 Comparative study of the photocatalytic performance for the degradation of different dyes by $ZnIn_2S_4$: adsorption, active species, and pathways *RSC Adv.* **7** 12292–300
[45] Fan Y *et al* 2012 Highly selective deethylation of rhodamine B on TiO_2 prepared in supercritical fluids *Int. J. Photoenergy* **2012** 173865 (1)-173685(7)
[46] Khataee A R, Fathinia M and Aber S 2010 Kinetic modeling of liquid phase photocatalysis on supported TiO_2 nanoparticles in a rectangular flat-plate photoreactor *Ind. Eng. Chem. Res.* **49** 12358–64
[47] Ji G, Shen H, Zhang J, Al-Saadi A A, Chang X, Ali M A, Zhou Q, Du M, Liu Y and Gondal M A 2012 Photodegradation of rhodamine B over unexcited semiconductor compounds of BiOCl and BiOBr *J. Colloid Interface Sci.* **377** 291–8
[48] Lee Y Y, Moon J H, Choi Y S, Park G O, Jin M, Jin L Y, Li D, Lee J Y, Son S U and Kim J M 2017 Visible-light driven photocatalytic degradation of organic dyes over ordered mesoporous $Cd_xZn_{1-x}S$ Materials *J. Phys. Chem.* C **121** 5137–44
[49] Ge S, Cai L, Li D, Fa W, Zhang Y and Zheng Z 2015 Daylight-driven photocatalytic degradation of ionic dyes with negatively surface-charged In_2S_3 nanoflowers: dye charge-dependent roles of reactive species *J. Nanoparticle Res.* **17** 488(1)-488(11)
[50] Chachvalvutikul A, Pudkon W, Luangwanta T, Thongtem T, Thongtem S, Kittiwachana S and Kaowphong S 2019 Enhanced photocatalytic degradation of methylene blue by a direct Z-scheme $Bi_2S_3/ZnIn_2S_4$ photocatalyst *Mater. Res. Bull.* **111** 53–60
[51] Li H, Deng Q, Liu J, Hou W, Du N, Zhang R and Tao X 2014 Synthesis, characterization and enhanced visible light photocatalytic activity of Bi_2MoO_6/Zn-Al layered double hydroxide hierarchical heterostructures *Catal. Sci. Technol.* **4** 1028–37
[52] Hong Y, Jiang Y, Li C, Fan W, Yan X, Yan M and Shi W 2016 *In-situ* synthesis of direct solid-state Z-scheme V_2O_5/g-C_3N_4 heterojunctions with enhanced visible light efficiency in photocatalytic degradation of pollutants *Appl. Catal. B Environ.* **180** 663–73